

# Section Force Correlation under Dynamic Wind Excitation of Balanced Cantilever Bridges

Martin N. Svendsen<sup>1</sup>, Sirwan Ghaderzadeh<sup>2</sup>

<sup>1</sup>Ramboll Denmark  
Hannemanns Alle 53, 2300 Copenhagen S, Denmark  
mnns@ramboll.dk

<sup>2</sup>Ramboll Norway  
Erik Børresens Allé 7, 3015 Drammen, Norway  
sirwan.ghaderzadeh@ramboll.no

**Abstract** - The design of the lower pylon and the foundation of large balanced cantilever bridges is often dominated by dynamic response to turbulent wind, and capacity verification relies heavily on cross-section analysis considering moment-force relations. This paper proposes a consistent method for general quantification of section force correlation effects, based on industry-standard response calculations in the frequency domain. The method implies that all possible combinations of any two section forces can be determined and considered in design verifications. Thus, the method can replace a simpler, and sometimes otherwise required approach where individually maximized components are assumed to act in full correlation. The method is verified using advanced time-domain wind response simulations, which allow for direct assessment of section force correlations. The adopted time-domain wind response simulations are fully consistent with the frequency-domain calculations and include accurate representation of turbulence coherence and motion-induced forces. Correlation regimes determined for displacements and different section force components using time- and frequency-domain calculations match closely, thus validating the proposed method. It is demonstrated for a generic 2x130m balanced cantilever that the presented method can lead to more cost-effective and sustainable solutions, e.g. via eccentric arrangement of internal prestressing in pylon legs.

**Keywords:** Structural dynamics, wind engineering, aerodynamics, balanced cantilever bridges, section force correlation.

## 1. Introduction

Long-span balanced cantilever bridges are generally prone to exhibit significant dynamic responses under turbulent wind loading, and the designs of foundations and lower pylons are often governed by this situation. Fig. 1 shows two examples of recent balanced cantilever projects, namely the Queensferry Crossing in Scotland with 2x322m cantilevers and the New Varodd Bridge in Norway with 130m+128m cantilevers. Ramboll was lead designer on both projects.

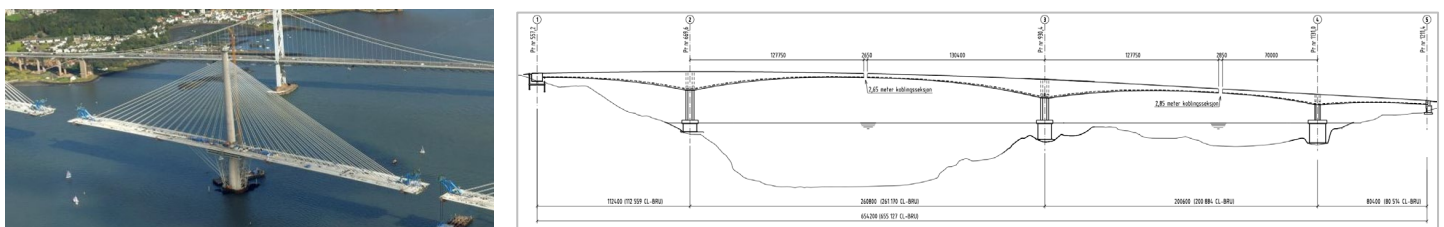


Fig. 1: Balanced cantilever examples. Left: Queensferry Crossing, Scotland. Right: New Varodd Bridge, Norway.

The design verification of e.g. the lower pylon relies heavily on cross-section analysis, including various combinations of section forces. Design codes rarely offer guidelines on how to account for correlation of section forces due to buffeting wind load. This implies that if such calculations are not performed, a conservative alternative may be to consider coexisting maximum values, e.g. to combine maximum bending moments about both axes of a cross-section, instead of one maximized and the other with its concurrent, and typically lower, value. This can however lead to sub-optimal designs and less

sustainable design solutions. This paper proposes a consistent method for general quantification of section force correlation effects, based on response calculations in the frequency domain. The method is based on a geometrically inspired vector projection, which allows for a general weighting of any two components under consideration. These could e.g. be a bending moment and a normal force, for use in M-N capacity verification.

The resulting correlation envelopes capture traditional results obtained by single-component maximization, but also all other possible combinations of the two components under consideration. The results are validated by advanced time-domain wind response simulations. The time simulations allow for direct assessment of section force correlations since these are readily available in every time step. The paper is structured as follows. In Sec. 2, a brief overview of the adopted frequency- and time-domain response assessment theory is given, and Sec. 3 provides a description of the generic balanced cantilever. Sec. 4 summarizes the adopted theory for wind simulation and shows the properties of the resulting turbulence field. In Sec. 5 the structural response is presented along with the proposed method for quantification of section force correlation effects. It is shown how an optimized cross-section design is obtained by considering the correlation properties mapped by the proposed method.

## 2. Theory

The wind response is determined by means of modal analysis in the frequency domain and by time simulation. The modal frequency-domain wind response theory corresponds to [1] and is briefly described in the following. The purely structural equations of motion are defined in configuration space as per Eq. (1a):

$$\mathbf{M}\ddot{\mathbf{x}} + \mathbf{C}\dot{\mathbf{x}} + \mathbf{K}\mathbf{x} = \mathbf{f} \quad (1a)$$

$$\tilde{\mathbf{M}}\dot{\mathbf{r}} + [\tilde{\mathbf{C}} - \tilde{\mathbf{C}}_a]\dot{\mathbf{r}} + [\tilde{\mathbf{K}} - \tilde{\mathbf{K}}_a]\mathbf{r} = \tilde{\mathbf{f}} \quad (1b)$$

where  $\mathbf{M}$  and  $\mathbf{K}$  are the structural mass and stiffness matrices and  $\mathbf{C}$  is the intrinsic damping matrix. From an eigenvalue analysis of the structural system, structural modal matrices  $\tilde{\mathbf{M}}$  and  $\tilde{\mathbf{K}}$  and  $\tilde{\mathbf{C}}$  can be established, whereby the modal equations of motion take the form of Eq. (1b). The matrices  $\tilde{\mathbf{C}}_a$  and  $\tilde{\mathbf{K}}_a$  are added modal aerodynamic damping and stiffness matrices, respectively. These matrices depend on frequency  $\omega$  and wind speed  $U$  and represent aerodynamic motion-induced forces, based on aerodynamic derivatives. Response variances  $\sigma^2$  are determined by integration of the absolute value of the response spectral densities as per Eq. (2a):

$$\sigma^2(U, \mathbf{x}) = \int_0^\infty |\mathbf{S}_R(U, \omega, \mathbf{x})| d\omega \quad (2a)$$

$$u_{i,\max} = \mu_{u_i} + \sigma_{u_i} k_p \quad (2b)$$

For a given wind speed  $U$  and at a given location  $\mathbf{x}$ , the total maximum response  $u_{i,\max}$ , e.g. the lateral displacement  $u_y$ , is determined as the sum of the static mean wind response  $\mu_{u_i}$  and the standard deviation of the turbulence response  $\sigma_{u_i}$  multiplied by the peak factor  $k_p$ , cf. Eq. (2b). The value  $k_p = 3.5$  is commonly accepted as a reasonable approximation, see e.g. [2]. Equation (2a) is a general, multi-modal representation. Integration of the dynamic wind response into the main FE-model of a given project is typically performed on a mode-by-mode basis where (2a) and subsequently (2b) are calculated mode by mode. The total response is then determined by SRSS combination as per Eq. (3a):

$$\alpha = \left[ \sum_j \alpha_j^2 \right]^{1/2} \quad (3a)$$

$$\alpha = \sum_j p_j \alpha_j \quad (3b)$$

where  $\alpha_j$  are modal standard deviations or peak values of a target component, e.g. a displacement or a section force, and  $\alpha$  is the maximized, scalar target value. For design purposes, it is often necessary to determine coexisting effects, such as bending moments coexisting with the maximum normal force. These can be determined via modal participation factors  $p_j$ , back-calculated from maximized scalar values as [3]:

$$p_j = \alpha_j / \alpha \quad (4)$$

These factors provide the weight of each mode in the combination, allowing for a second modal superposition where all effects coexisting with the maximized scalar value are determined, cf. Eq. (3b). A typical set of target scalar values for an

M-N cross-section verification consists of the six section force components, and axial corner stresses. This is discussed further in Sec. 5.

The time-domain wind response theory corresponds to [4] and is briefly described in the following. One challenge with time-domain response calculations relates to the representation of motion-induced aerodynamic forces. These are typically determined by wind tunnel tests and reported as aerodynamic derivatives. These aerodynamic derivatives are frequency-dependent which implies that they cannot be adopted directly for time integration. A full account of these effects involves the calculation of a convolution integral which is computationally expensive and impractical for aerodynamic implementation. However, the aeroelastic effects can be included with good accuracy in the form of additional state-space variables, governed by first order differential equations found via rational approximations of the aerodynamic derivatives. The aeroelastic equations of motion take the form of Eq. (5a):

$$\begin{bmatrix} \mathbf{C} & \mathbf{M} & \mathbf{0} \\ \mathbf{M} & \mathbf{0} & \mathbf{0} \\ \mathbf{0} & \mathbf{0} & \mathbf{I}_{j \times j} \end{bmatrix} \begin{bmatrix} \dot{\mathbf{q}} \\ \dot{\mathbf{v}} \\ \dot{\mathbf{f}} \end{bmatrix} + \begin{bmatrix} \mathbf{K} & \mathbf{0} & -\mathbf{I}_{1 \times j} \\ \mathbf{0} & -\mathbf{M} & \mathbf{0} \\ -\mathbf{D} & \mathbf{0} & \mathbf{\Gamma} \end{bmatrix} \begin{bmatrix} \mathbf{q} \\ \mathbf{v} \\ \mathbf{f} \end{bmatrix} = \begin{bmatrix} \mathbf{f}_e \\ \mathbf{0} \\ \mathbf{0} \end{bmatrix} \quad (5a) \quad \mathbf{D} = \begin{bmatrix} \mathbf{D}_1 \\ \vdots \\ \mathbf{D}_N \end{bmatrix}, \mathbf{\Gamma} = \begin{bmatrix} \gamma_1 \mathbf{I} & \dots & \mathbf{0} \\ \vdots & \ddots & \vdots \\ \mathbf{0} & \dots & \gamma_N \mathbf{I} \end{bmatrix}, \mathbf{f} = \begin{bmatrix} \mathbf{f}_1 \\ \vdots \\ \mathbf{f}_N \end{bmatrix} \quad (5b)$$

with the aerodynamic terms represented in Eq. (5b), corresponding to the first order differential equation  $\dot{\mathbf{f}}_j + \gamma_j \mathbf{f}_j = \mathbf{D}_j \mathbf{q}$ , where  $\mathbf{f}_j$  are self-excited aerodynamic forces, the matrices  $\mathbf{D}_j$  represent the aerodynamic cross-section properties and  $\gamma_j$  are the memory decay factors relating to an assumed exponential form of the convolution kernel. Time integration is performed by a momentum-based procedure, in which the first order differential equations of the aerodynamic system are integrated over a time increment, leading to a discretized set of equations.

### 3. Balanced cantilever

The present investigations are performed for a 2x130m balanced cantilever with simplified, constant cross-section properties, chosen to obtain realistic dynamic properties of the system. The girder mass is  $m_g = 2.67e4\text{kg/m}$  and its bending stiffnesses are  $EI_y = 2.76e12\text{Nm}^2$  and  $EI_z = 1.55e14\text{Nm}^2$ . The central pier consists of two separate post-tensioned concrete legs, similar to the example in Fig. 1b. The cross-sections of these, including longitudinal reinforcement and post-tensioning, are shown in Fig. 2a. The total tensioning force per leg is  $8 \times 3.75\text{MN} = 30\text{MN}$ . In Fig. 2b the first two still-air eigenmodes are shown. Mode 1 is dominated by transverse girder displacements and will generate out-of-plane bending  $M_z$  and shear  $Q_y$  in the pier legs. Mode 2 is dominated by vertical girder displacements and will generate normal forces  $N$  and in-plane bending moments  $M_y$  in the pier legs.

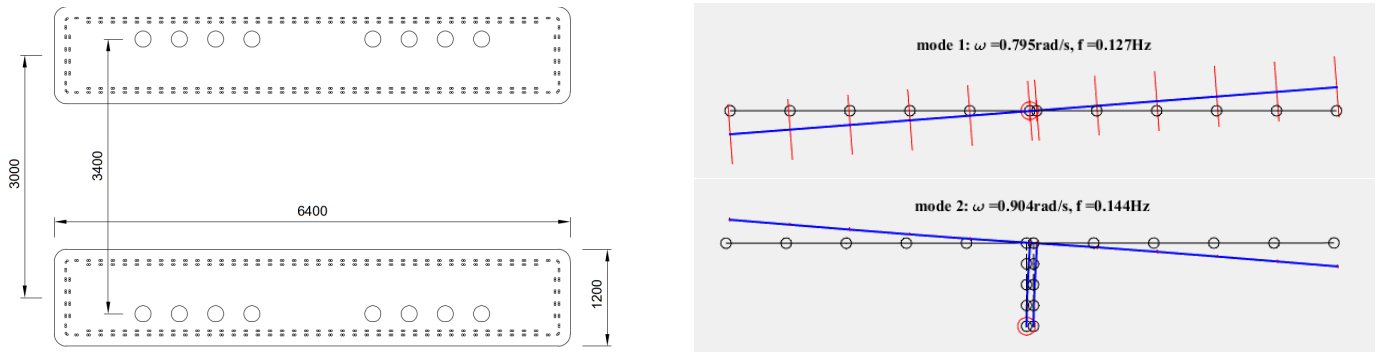


Fig. 2: a) Cross-sections of the two pier legs. b) The first two eigenmodes of the balanced cantilever.

Wind loads are considered for the girder only. Aerodynamic coefficients are chosen as  $C_D = 1.2$ ,  $C_L = -0.15$ ,  $C_L' = 6.3$ ,  $C_M = 0.30$ ,  $C_M' = 1.0$  with the reference cross-wind dimension  $D = 2.5\text{m}$  and the along-wind dimension  $B = 13\text{m}$ . Motion-induced forces are modelled using aerodynamic derivatives corresponding to flat plate theory. Structural damping is represented by Rayleigh damping, calibrated to  $\zeta = 0.0032$  for mode 1 and 2. The corresponding modal damping ratios are adopted in the modal frequency domain analysis.

## 4. Wind field

The bridge response is investigated using an anisotropic form of the full-field sequential simulation procedure [5]. The normalized von Karman auto-spectrum is adopted as per Eq. (6a) with  $k = \omega/U$  and  $l_u = 1.339L_x^u$ . The normalized form enables derivation of explicit coherence functions but is in practice mostly used in the form given in Eq. (6b).

$$S_{uu}(k) = \frac{1}{\sqrt{\pi}} \frac{\Gamma(5/6)}{\Gamma(1/3)} \frac{l_u \sigma_u^2}{[1 + (1 + kl_u)^2]^{5/6}} \quad (6a) \quad S_{uu,p}(f) = \frac{4\sigma_u^2 f_u}{[1 + 70.8f_u^2]^{5/6} f}, f_u = \frac{f L_x^u}{U} \quad (6b)$$

The longitudinal length scale is  $L_x = 300\text{m}$  and the transverse and vertical length scales are taken as  $L_y = L_z = 1/2L_x$ . The mean wind speed is  $U = 37\text{m/s}$ , the longitudinal turbulence intensity is  $I_u = 0.14$  and the transverse and vertical turbulence intensities are  $I_v = I_w = 1/2I_u$ . The differences in length scales and turbulence intensities are achieved as stretched isotropic turbulence as described in [5].

The turbulence components are realized in every girder node of the structural FE-model and in Fig. 3a, extracts of time histories for the longitudinal and vertical turbulence components are shown for the left girder end node. In Fig. 3b the auto-spectral density  $S_{uu}$  of the longitudinal turbulence component  $u$  is shown, both in terms of the target spectrum and the spectrum of the simulated wind at a single location. It is seen that the target spectrum is matched well, and a similar result is obtained for the vertical component.

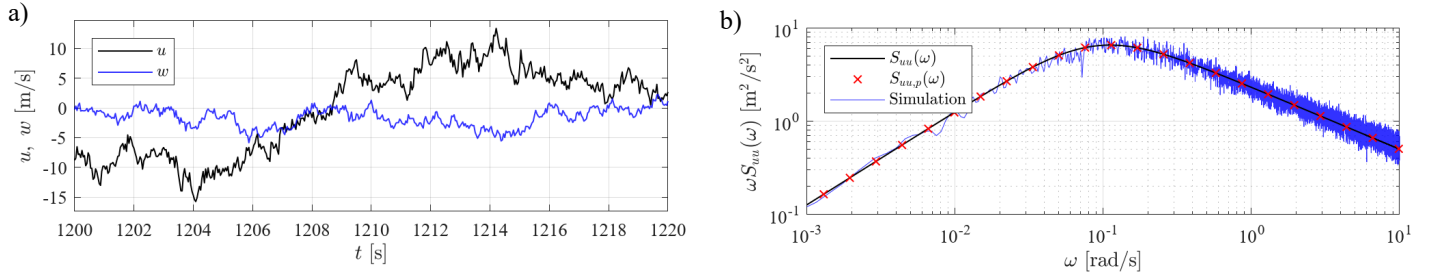


Fig. 3: a) Wind velocity records. b) Auto-spectral density  $S_{uu}$ .

The transverse coherence functions  $\psi_{ij}$  are explicitly defined, where Eq. (7a) shows the expression for the longitudinal turbulence, with angular frequency  $\omega$  and separation  $r$ :

$$\psi_{uu}(\omega, r) = \frac{2}{\Gamma(\gamma)} \left[ \left( \frac{\kappa_1 r}{2} \right)^\gamma K_\gamma(\kappa_1 r) - \left( \frac{\kappa_1 r}{2} \right)^{\gamma+1} K_{\gamma-1}(\kappa_1 r) \right] \quad (7a) \quad \psi_{ij,N400}(f, r) = \exp(-C_{ij} fr/U) \quad (7b)$$

In Eq. (7a),  $K_\gamma$  and  $K_{\gamma-1}$  are modified Bessel functions and  $\kappa_1^2 = (\omega/U)^2 + l_u^{-2}$ . Target and measured coherences of the longitudinal and vertical turbulence components are shown in Fig. 4 and good agreement is achieved. For comparison, the Davenport exponential format adopted e.g. in the Norwegian Standard [6], given as Eq. (7b) is also plotted. It is seen that the simulated wind field captures both the absence of full correlation at vanishing frequency, and negative coherence in line with the basic zero-mean assumption.

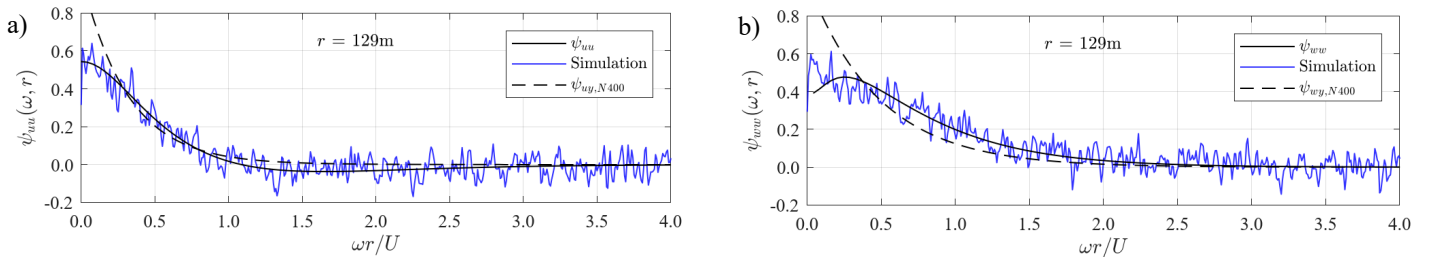


Fig. 4: Coherences, transverse separation. a) Longitudinal turbulence. b) vertical turbulence.

As discussed in [5], long simulations are necessary to obtain well-converged steady-state responses which are necessary for validation against frequency-domain results. In the present case, a single 60-hour simulation was used for the spectral wind field analyses and a single 10-hour simulation was used for the response analyses. Both simulations were preceded by a 1200s initial phase for decay of transient effects.

## 5. Response envelopes

Convergence of the modal frequency-domain analysis was obtained with inclusion of 5 modes. In Fig. 5a, time history extracts of transverse displacements  $u_y$  and vertical displacements  $u_z$  for the left end of the cantilever are shown. The transverse displacements are dominated by mode 1 excitation while the vertical displacements contain more harmonics.

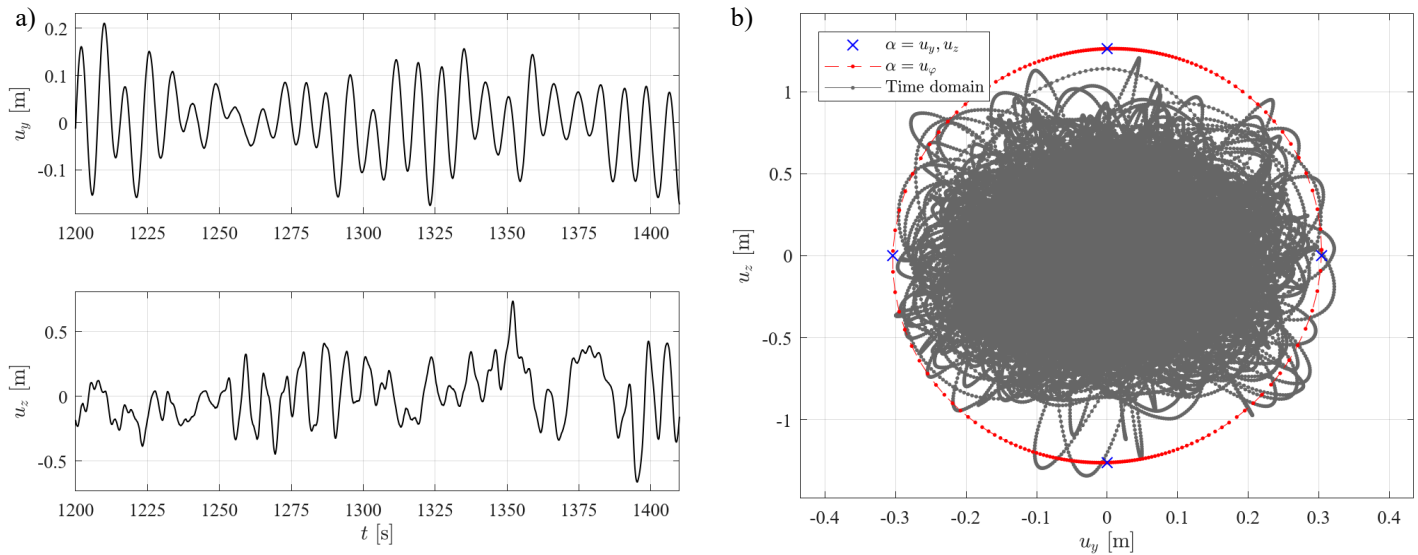


Fig. 5: a) Cantilever tip displacements. b)  $u_y$ - $u_z$  diagram, char. wind effects.

As a validation, a comparison of time-domain (TD) and modal frequency-domain (MFD) results is shown in Table 1, in terms of standard deviations with frequency domain results as reference. Good agreement is achieved, with time domain results slightly overestimating transverse and vertical displacements by 0.4% and 4.5% respectively. This level of agreement is considered acceptable and compares well with e.g. [7]. Peak values corresponding to the last 10x10 minutes of the simulation are also shown in the table. These values compare reasonably well with the typical value of  $k_p = 3.5$ . The peak values depend on the length of the simulation, which implies that for direct comparison of peak time- and frequency-domain results, peak factors obtained from the time domain analysis must be used for assessment of peak values of the frequency domain results.

Table 1. MFD/TD standard deviations and peak factors.

	MFD	TD	Deviation [%]	$k_p$ (max)	$k_p$ (max)
$u_y$ [mm]	96	96	0.4	3.2	2.9
$u_z$ [mm]	307	321	4.5	3.7	4.1

The cantilever end displacements excluding the mean wind effect are visualized in Fig. 5b. In this plot, all values from the time domain simulation are included. In addition, peak displacements  $u_y$  and  $u_z$  determined by the modal frequency-domain calculation are shown as four blue crosses, capturing both positive and negative values. Peak factors obtained from the time simulation are used and as also shown in Table 1, the agreement between the two calculation methods is good.

It is evident from Fig. 5b that the individual SRSS maximization of the two displacement components does not capture the entire displacement field, because combinations of the two exist as well. It is of interest to quantify the potential combinations of  $u_y$  and  $u_z$ , e.g. to determine if the individual maximum values of  $u_y$  and  $u_z$  can occur simultaneously. The full range of possible combinations of  $u_y$  and  $u_z$  can be determined from the modal results by maximizing the resultant of

the two components as described in the following. For a given mode  $j$ , the standard deviation displacement vector  $\mathbf{u}_j$  is defined as per Eq. (8a):

$$\mathbf{u}_j = \begin{bmatrix} u_{y,j} \\ u_{z,j} \end{bmatrix} \quad (8a)$$

$$u_{\varphi,j} = \mathbf{u}_j^T \mathbf{e}_\varphi, \quad \mathbf{e}_\varphi = \begin{bmatrix} \cos\varphi \\ \sin\varphi \end{bmatrix} \quad (8b)$$

The modal displacement  $u_{\varphi,j}$  in any given direction  $\varphi$  in the  $y$ - $z$  plane can then be written as the projection of the modal displacement vector on to the unit vector  $\mathbf{e}_\varphi$ , which is oriented in the direction of interest, cf. Eq. (8b). The modal scalar maximization target  $\alpha_j$  for the SRSS combination, according to the general definition (3a), then follows as Eq. (9):

$$\alpha_j = u_{\varphi,j} = \mathbf{u}_j^T \mathbf{e}_\varphi \quad (9)$$

For  $\varphi = 0$  and  $\varphi = \pi/2$ , individual maximization of  $u_y$  and  $u_z$  is reproduced, and for the general case  $0 \leq \varphi < 2\pi$  the maximum SRSS displacement  $u_\varphi$  in any direction  $\varphi$  can be obtained. For any  $u_\varphi$  a corresponding set of modal participation factors can be determined according to (4). From these modal participation factors, corresponding displacements  $\mathbf{u} = [u_y \ u_z]^T$ , section forces or stresses can be determined via (3b). In Fig. 5b, peak displacements  $\mathbf{u}$  corresponding to different values of  $\varphi$  are shown as red dots. The peak displacements are determined using peak factors from the time simulation, cf. Table 1. Each red dot represents a given angle  $\varphi$ , with a unique set of modal participation factors corresponding to  $u_\varphi$ . The displacements  $\mathbf{u}$  are seen to envelope the time simulation results well. It is also clear, both from the displacements  $\mathbf{u}$ , corresponding to  $u_\varphi$ , and the time simulation results, that maximum values of  $u_y$  and  $u_z$  respectively, do not occur simultaneously.

For design of line-like structural members it is relevant to have similar information about cross-section forces. In the following, the effects in the left pier leg are considered. A typical design check involves determination of maximum section forces as per target definitions in Eq. (10a) and maximum axial corner stresses as per the target definition in Eq. (10b). The calculation of maximum axial corner stresses is relevant for crack width checks and is also an approximate way of capturing two-axis bending effects.

$$\alpha_j = N_j, \alpha_j = M_{y,j}, \alpha_j = M_{z,j} \quad (10a)$$

$$\alpha_j = \sigma_{xx,j} = \frac{N_j}{A} + \frac{M_{z,j}}{I_z} y - \frac{M_{y,j}}{I_y} z \quad (10b)$$

In Fig. 6a and 6b, section force combinations are plotted as peak values in  $M_y$ - $N$  and  $M_z$ - $N$  relations respectively. Compression corresponds to  $N < 0$ . Peak factors for section forces from time simulations are adopted, taking the largest value from maximum and minimum results respectively. The values according to section force maximization, i.e. Eq. (10a), are plotted as blue circles. Each circle represents the maximized (or minimized) value with its coexisting value.

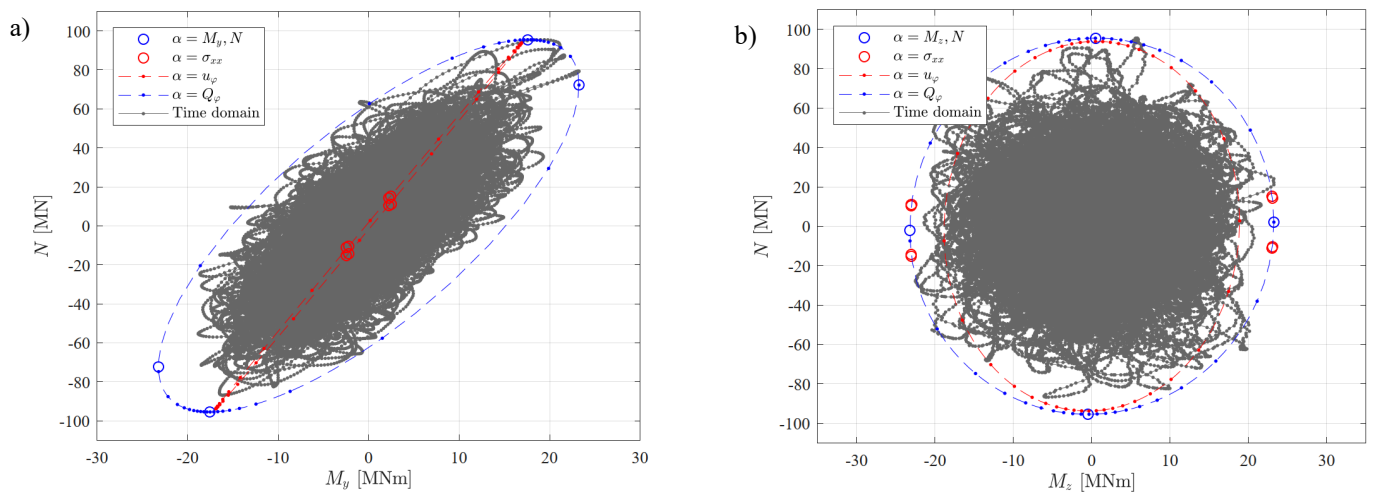


Fig. 6: M-N diagrams for turbulent wind response (mean wind excluded). a)  $M_y$ - $N$ . b)  $M_z$ - $N$ .

It is seen in Fig. 6a that the maximum normal force  $N$  occurs together with a relatively high in-plane bending moment  $M_y$  and vice versa. This is because these two values are mainly generated by mode 2, i.e. they are strongly correlated. Oppositely, in Fig. 6b it is seen that the maximum normal force  $N$  occurs together with a relatively small out-of-plane bending moment  $M_z$  and vice versa. This reflects the fact that the normal force  $N$  is mainly generated by mode 2 and the out-of-plane bending moment  $M_z$  is mainly generated by mode 1. This implies that  $N$  and  $M_z$  are less correlated. The values according to stress maximization are shown as red circles. It is seen that the largest corner stresses are found for modal combinations with emphasis on  $M_z$  while  $N$  and  $M_y$  are less pronounced in this regard and thus provide non-relevant values for the  $M_y$ - $N$  verification.

The blue and red circles represent typical result sets determined for cross-section verification. The locations of these points in the diagrams might indicate that all possible M-N combinations are located within a somewhat elliptical envelope which passes through these. In other words, indications are that maximum bending moments and the maximum normal force will not occur simultaneously. In Fig. 6a-b, section forces from the time simulation are also shown and these support the hypothesis of elliptical envelopes. Since time simulations are typically not available in practical design situations, an envelope of section force correlation based on the modal frequency-domain calculation is desirable. This is developed in the following.

To determine the full range of possible combinations of  $M$  and  $N$ , a maximization similar to that of the end displacement combinations (9) is considered, namely as a vector projection along a given direction  $\varphi$  in the M-N plane. The modal scalar maximization target takes the form:

$$\alpha_j = Q_{\varphi,j} = \mathbf{Q}_j^T \mathbf{e}_\varphi \quad , \quad \mathbf{Q}_j^T = [M_{k,j} \ N_j] \quad (11)$$

with  $k = y, z$ . As for the similar form of the displacement target, this reproduces individual maximization of  $M_k$  and  $N$  for  $\varphi = 0$  and  $\varphi = \pi/2$ . In Fig. 6a-b, peak values corresponding to different values of  $\varphi$  are shown as blue dots connected by a dashed blue line. Again, each dot represents a given angle  $\varphi$ , with a unique set of modal participation factors corresponding to  $Q_\varphi$ . The results confirm the expected elliptical envelopes and prove, also via frequency domain analysis, that maximum moments and maximum normal forces will not coexist. Fig. 6a-b also show values coexisting with  $u_\varphi$ , marked (as in Fig. 5b) with red dots connected with red dashed lines. It is seen that the maximization for  $u_\varphi$  provides M-N combinations which only partially capture the critical values. This underlines the necessity of (11) to fully envelope all possible M-N combinations.

As a validation, Table 2 compares MFD and TD section forces and it is seen that good agreements are achieved, although with slightly higher deviations than achieved for displacements.

Table 2. MFD/TD section force standard deviations.

	$N$ [MN]	$Q_y$ [MN]	$Q_z$ [MN]	$M_x$ [MNm]	$M_y$ [MNm]	$M_z$ [MNm]
MFD	24.2	0.32	0.25	8.69	5.64	6.73
TD	25.8	0.32	0.23	9.20	5.38	5.92
Dev. [%]	6.5	1.2	-5.9	5.9	-4.6	-12.0

The higher deviations for section forces compared with displacements may be due to more pronounced model differences in the representation of high-frequency content, e.g. in relation to the spatial resolution of the time-domain model.

The ULS design verification of a concrete cross-section such as the concrete pier leg cross-section will involve plotting design loads together with M-N capacity contours. In Fig. 7a-b such diagrams are shown, assuming a normal force of  $N_g = -65$  MN due to self-weight and post-tensioning and an out-of-plane bending moment due to mean wind of  $M_{z,m} = 13.8$  MN. Further, the eccentric placement of the post-tensioning cables leads to a permanent in-plane moment  $M_{y,PT} = -6$  MNm. The capacity contours represent reinforcement arrangements of 4 or 2  $\varnothing 25$  mm bars per 150 mm along the edge of the cross-section.

A simplified design approach assuming fully correlated maximum values determined via Eq. (10a) is represented as points A-D and E-H. In Fig. 7a it is seen that the design based on Eq. (11) has sufficient capacity. In the present case, the eccentric placement of the post-tensioning is instrumental in limiting positive values of  $M_y$ . If the more conservative design approach of point A-D were considered, then the design would erroneously not pass due to point B exceeding capacity, and material additions such as increased reinforcement quantities or cross-section dimensions would become necessary.

As per typical practice, the present design example seeks the limit of the tensile capacity while keeping a larger margin to the compressive capacity. A slightly larger margin to the compressive capacity than shown here would normally be sought, but small margins are kept in the present case to better illustrate the relevant principles.

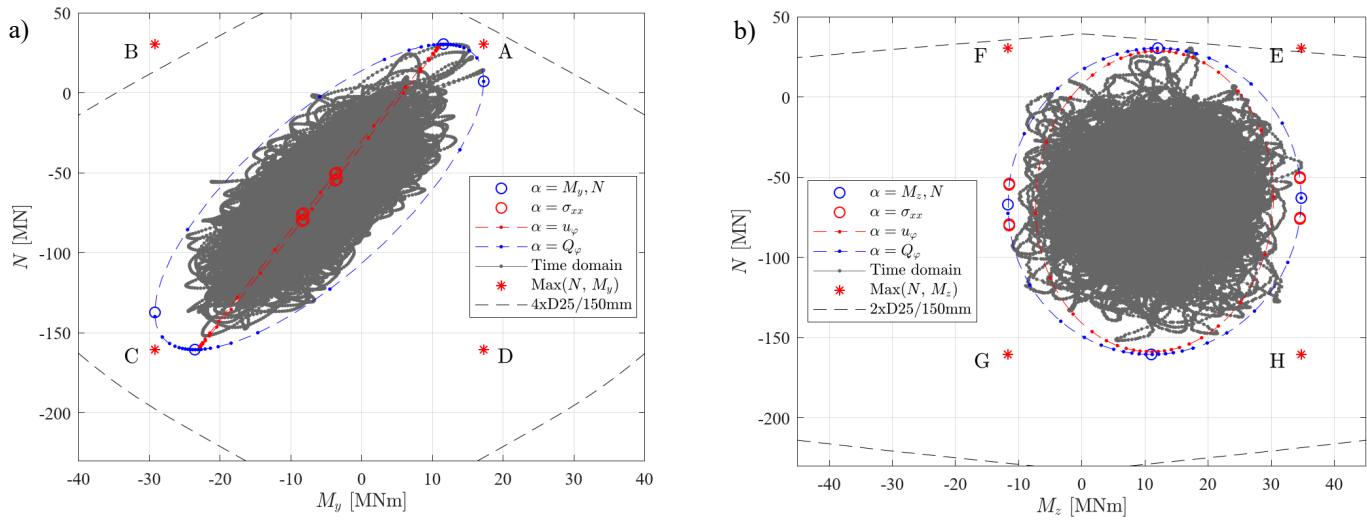


Fig. 7: ULS design verification diagrams. a)  $M_y$ - $N$ . b)  $M_z$ - $N$ .

The target definition in (11) could potentially be expanded to determine an  $M_y$ - $M_z$ - $N$  correlation surface. Further, the method is independent of structural type and could therefore also be used for assessment of e.g. steel girder capacity.

## 6. Conclusions

In the present paper, a method for accurately enveloping section force correlation, based on modal frequency-domain response calculations is proposed and validated by direct time-simulation. The investigation is performed for a simplified balanced cantilever. It is demonstrated that the method in some cases may allow for significant cross-section optimization and material savings, e.g. via eccentric arrangement of internal prestressing in pier legs.

## Acknowledgements

The present work was funded by the Ramboll Denmark Knowledge and Innovation Board, the Bridges department in Norway, the Major Bridges department in Denmark, and the Major Crossings Spearhead Division.

## References

- [1] O. Øiseth, A. Rönnquist, and R. Sigbjörnsson, "Simplified prediction of wind-induced response and stability limit of slender long-span suspension bridges, based on modified quasi-steady theory: A case study", *Journal of Wind Engineering and Aerodynamics*, 98, p. 730-741, 2010.
- [2] A. Larsen, G. Larose, "Dynamic wind effects on suspension and cable-stayed bridges", *Journal of Sound and Vibration*, 2015.
- [3] C. Katz, "Anmerkung zur Überlagerung von Antwortspektren", *DACH Mitteilungsblatt*, vol. 84, 2009.
- [4] R. N. Møller, S. Krenk, M. N. Svendsen, "Time simulation of aerodynamic response of long-span bridges to turbulent wind", *Journal of Wind Engineering & Industrial Aerodynamics*, vol. 199, 2020.
- [5] S. Krenk, R. N. Møller, "Turbulent wind field representation and conditional mean-field simulation", *Proceedings of the Royal Society*, vol. 475, 2019.
- [6] Norwegian Public Roads Administration, "Bruprojektering N400", 2015.
- [7] K. Aas-Jakobsen, E. Strømmen, "Time domain buffeting response calculations of slender structures", *Journal of Wind Engineering and Industrial Aerodynamics*, 89, p. 341-364 2001.